Applications of Mathematics

Nicola Botta; Rolf Jeltsch
A numerical method for unsteady flows

Terms of use:

A NUMERICAL METHOD FOR UNSTEADY FLOWS

Nicola Botta, Rolf Jeltsch, Zürich

Summary. A high resolution finite volume method for the computation of unsteady solutions of the Euler equations in two space dimensions is presented and validated. The scheme is of Godunov-type. The first order part of the flux function uses the approximate Riemann problem solver of Pandolfi and here a new derivation of this solver is presented. This construction paves the way to understand the conditions under which the scheme satisfies an entropy condition. The extension to higher order is done by applying ideas of LeVeque to the approximate Riemann problem solution. A detailed validation of the scheme is done on one and two dimensional test problems.

Keywords: finite volume method, Euler equations, Riemann problem

AMS classification: 65M05, 05M25, 65M99, 76H05, 76K05

1. INTRODUCTION

The aim of this paper is to present and validate a finite volume method for the numerical computation of unsteady solutions of the Euler equations in two space dimensions. The method is based on the approximate solution of Riemann problems at the interfaces between the cells of the discretization.

In section 2 we present the numerical method. The flux function is derived in section 2.1. Here it is shown that the cell averages obtained with the first order flux function proposed by Pandolfi in [15] can be interpreted as the averages of a (possibly multi-valued) "function". This "function" can be constructed by piecing together the solutions of special Riemann problems. With this interpretation it is easy to understand under which conditions the method satisfies an entropy condition. In 2.2 a high resolution method is derived following the ideas presented in [9] and in the frame of the Riemann problem solver described in 2.1. In 2.3 the treatment of the boundaries is shortly addressed.

Section 3 is devoted to the validation of the method. Validation criteria are discussed and applied to typical one and two dimensional test problems. A one dimen-

sional problem is envisaged to check the boundary conditions and the capability of the method to correctly describe the behaviour of the flow at large times.

2. THE NUMERICAL METHOD

Let $\mathscr{D} \times [0, T]$ be a closed subset of $\mathbb{R}^2 \times \mathbb{R}^+$, $\mathscr{C} \subset \mathscr{D}$ an open set in $\mathscr{D}$ and $\partial \mathscr{C}$ the boundary of $\mathscr{C}$. Let $\mathscr{C}$ be fixed in time and $t^0, t^1 \in [0, T]$. The physical principles of conservation of mass, momentum and energy can be written in the following integral form

$$(1) \qquad \int_{\mathscr{C}} \mathbf{U}(\mathbf{x}, t^1) \, \mathrm{d}A = \int_{\mathscr{C}} \mathbf{U}(\mathbf{x}, t^0) \, \mathrm{d}A - \int_{t^0}^{t^1} \int_{\partial \mathscr{C}} \mathbf{F}(\mathbf{U}(\mathbf{x}, t), \mathbf{n}(\mathbf{x})) \, \mathrm{d}l \, \mathrm{d}t.$$

The second principle of thermodynamics reads

$$(2) \qquad \int_{\mathscr{C}} S(\mathbf{U}(\mathbf{x}, t^1)) \, \mathrm{d}A \geqslant \int_{\mathscr{C}} S(\mathbf{U}(\mathbf{x}, t^0)) \, \mathrm{d}A - \int_{t^0}^{t^1} \int_{\partial \mathscr{C}} S(\mathbf{U}(\mathbf{x}, t)) \mathbf{u}(\mathbf{U}(\mathbf{x}, t)) \cdot \mathbf{n}(\mathbf{x}) \, \mathrm{d}l \, \mathrm{d}t.$$

In (1), (2) $\mathbf{x} \in \mathscr{C}$ is the space coordinate, $t \in [0, T]$ is the time and $\mathrm{d}A$, $\mathrm{d}l$ and $\mathrm{d}t$ are elements of area, length and time, respectively. The vector function of the conserved variables $\mathbf{U}$ and the vector function of the fluxes $\mathbf{F}$ are

$$(3) \qquad \mathbf{U} = \begin{pmatrix} \varrho \\ \varrho \mathbf{u} \\ \varrho e \end{pmatrix} \quad \text{and} \quad \mathbf{F} = \begin{pmatrix} \varrho(\mathbf{u} \cdot \mathbf{n}) \\ p\mathbf{n} + \varrho \mathbf{u}(\mathbf{u} \cdot \mathbf{n}) \\ (\varrho e + p)(\mathbf{u} \cdot \mathbf{n}) \end{pmatrix}.$$

ϱ is the density, $\mathbf{u}$ the velocity, e the internal specific energy and p the pressure. S is the entropy per unit volume, $S(\mathbf{U}(\mathbf{x}, t)) = s(\mathbf{U}(\mathbf{x}, t))\varrho(\mathbf{U}(\mathbf{x}, t))$, and s the specific entropy. Pressure and specific entropy depend on $\mathbf{U}(\mathbf{x}, t)$ through the *state equations*

$$(4) \qquad p = \varrho(\gamma - 1)\left(e - \frac{1}{2}\mathbf{u} \cdot \mathbf{u}\right) \quad \text{and} \quad s = \frac{R}{\gamma - 1} \ln \frac{p}{\varrho^\gamma}.$$

Notice that, if $\mathbf{U}(\mathbf{x}, t)$ is smooth in $\mathscr{C}$, then (1) $\Rightarrow$ (2) with the sign of equality.

One seeks, for given initial and boundary conditions, a function $\mathbf{U}(\mathbf{x}, t)$ satisfying both (1) and (2) for each $\mathscr{C} \subset \mathscr{D}$, $[t^0, t^1] \subset [0, T]$.

Let $\mathbf{x} = (x, y)$ and $\mathbf{u} = (u, v)$. Let $\mathscr{D}$ be discretized with a Cartesian grid of grid spacing h and let x_i and y_j be the x and the y coordinates of the interfaces normal to the coordinate directions with $i = 1, \ldots, ni$ and $j = 1, \ldots, nj$ (figure 1, left).

Let $\mathbf{U}_{i,j}^n$ be a numerical approximation to the *exact* cell averages

$$(5) \qquad \frac{1}{h^2} \int_{x_i}^{x_{i+1}} \int_{y_j}^{y_{j+1}} \mathbf{U}(x, y, t^n) \, \mathrm{d}y \, \mathrm{d}x.$$
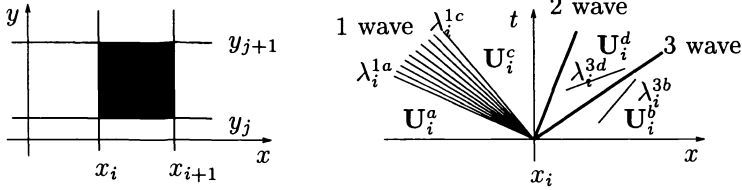
Fig. 1. Grid (left) and solution of the one-dimensional Riemann problem at $x = x_i$ (right).

A finite volume split method for (1) has the form

$$(6) \qquad \mathbf{U}_{i,j}^{n+1} = I_y(k) I_x(k) \mathbf{U}_{i,j}^n$$

where I_x and I_y are the operators

$$(7) \qquad I_x(k) : \mathbf{U}_{i,j}^n \rightarrow \mathbf{U}_{i,j}^n - \frac{k}{h} \left[\mathbf{F}_{i+1,j} - \mathbf{F}_{i,j} \right] \quad \text{and}$$

$$(8) \qquad I_y(k) : \mathbf{U}_{i,j}^n \rightarrow \mathbf{U}_{i,j}^n - \frac{k}{h} \left[\mathbf{G}_{i,j+1} - \mathbf{G}_{i,j} \right],$$

k is the time step and the *numerical fluxex* $\mathbf{F}_{i+1,j}$, $\mathbf{F}_{i,j}$ and $\mathbf{G}_{i,j+1}$, $\mathbf{G}_{i,j}$ are computed by considering one-dimensional problems in the x and in the y direction, respectively.

One would like to compute the numerical fluxes in such a way that the following properties hold

 (i) Smooth solutions are computed with second order accuracy.
 (ii) Discontinuities are captured with no oscillations and with minimal smearing.
 (iii) If the numerical solution converges, for $h \rightarrow 0$, towards a weak solution of (1), then this solution satisfies (2) as well.

Godunov's method [8] provides numerical fluxes for which (ii) and (iii) hold. In this method $\mathbf{F}_{i,j}$ is computed by solving the one-dimensional Riemann problem

$$(9) \qquad \int_a^b \mathbf{U}(x, t^1) \, dx = \int_a^b \mathbf{U}(x, t^0) \, dx - \int_{t^0}^{t^1} [\mathbf{F}(\mathbf{U}(b,t)) - \mathbf{F}(\mathbf{U}(a,t))] \, dt.$$

with initial data at time t^n

$$(10) \qquad \mathbf{U}(x, t^n) = \begin{cases} \mathbf{U}_{i-1,j}^n & \text{for} \quad x < x_i \\ \mathbf{U}_{i,j}^n & \text{for} \quad x > x_i. \end{cases}$$

and $[t^0, t^1] \subset [t^n, T]$, $[a, b] \subset [x_1, x_{ni}]$ (figure 1, right). In (9) $\mathbf{F}(\mathbf{U}(a,t))$ has been used instead of $\mathbf{F}(\mathbf{U}(a,t), (1,0))$ since it is clear that we are considering a Riemann

problem in the x direction. Let $\mathbf{U}_i(x,t)$ be the entropy satisfying solution[1] of this Riemann problem. $\mathbf{F}_{i,j}$ is computed by evaluating $\mathbf{F}(\mathbf{U}_i(x,t))$ at $x = x_i$ and $t > t^n$. This can be done directly because the solution of the Riemann problem is constant along rays $\lambda = (x - x_i)/(t - t^n)$

$$(11) \qquad \mathbf{F}_{i,j} = \mathbf{F}(\mathbf{U}_i(x_i,t)), \quad t > t^n.$$

Since $\mathbf{U}_i(x,t)$ is a solution of (9) $\mathbf{F}_{i,j}$ can also be computed using (9) with $[a,b] \times [t^0,t^1] = [x_i - h/2, x_i] \times [t^n, t^n + k]$. The computation is particularly easy if k is chosen so that $\mathbf{U}_i(x_i - h/2, t) = \mathbf{U}^n_{i-1,j}$ for $t \in [t^n, t^n + k]$. In this case (9) yields

$$(12) \qquad \mathbf{F}_{i,j} = \mathbf{F}(\mathbf{U}^n_{i-1,j}) + \frac{h}{2k}\mathbf{U}^n_{i-1,j} - \frac{1}{k}\int_{x_i-h/2}^{x_i}\mathbf{U}_i(x, t^n + k)\,\mathrm{d}x$$

or

$$(13) \qquad \mathbf{F}_{i,j} = \mathbf{F}(\mathbf{U}^n_{i,j}) - \frac{h}{2k}\mathbf{U}^n_{i,j} + \frac{1}{k}\int_{x_i}^{x_i+h/2}\mathbf{U}_i(x, t^n + k)\,\mathrm{d}x.$$

In (13) $\mathbf{F}_{i,j}$ has been computed integrating over $[a,b] \times [t^0,t^1] = [x_i, x_i + h/2] \times [t^n, t^n + k]$.

2.1. Numerical flux function.

Consider again the Riemann problem (9) with initial data (10). The solution $\mathbf{U}_i(x,t)$ can be easily computed once it is known whether the acoustic waves issuing from the breakdown of the discontinuity at $x = x_i$ are entropy satisfying shocks or rarefaction waves. This problem can be easily solved because of the fact that, in the phase space, a solution consisting of two rarefaction waves and of a contact discontinuity always exists.

Let $\mathbf{U}^a_i = \mathbf{U}^n_{i-1,j}$, $\mathbf{U}^b_i = \mathbf{U}^n_{i,j}$ and $\mathbf{U}^c_i$, $\mathbf{U}^d_i$ be the unknown intermediate states of the solution of the Riemann problem at $x = x_i$ (figure 1, right). Let $\mathbf{V}$ be the vector function of the variables (a, u, v, s) with $a^2 = \gamma p/\varrho$ (a is the *speed of sound*).

Using a 1 rarefaction wave to connect $\mathbf{V}^c_i$ to $\mathbf{V}^a_i$ (here $\mathbf{V}^c_i$ means $\mathbf{V}(\mathbf{U}^c_i)$, of course) and a 3 rarefaction wave to connect $\mathbf{V}^d_i$ to $\mathbf{V}^b_i$ one has

$$(14) \qquad \mathbf{V}^c_i = \mathbf{V}^{r_1}(\alpha, \mathbf{V}^a_i) \quad \text{and} \quad \mathbf{V}^d_i = \mathbf{V}^{r_3}(\beta, \mathbf{V}^b_i)$$

where α and β are given by the straightforward solution of the system

$$s^b_i = s^a_i + \frac{2}{\gamma-1}R\log\frac{1}{\sqrt{1+\mu}} - R\log(1+\mu)$$

$$(15) \qquad u^a_i + \frac{2}{\gamma+1}\alpha = u^b_i + \frac{2}{\gamma+1}\beta \qquad a^b_i + \frac{\gamma-1}{\gamma+1}\beta = \frac{(a^a_i - \frac{\gamma-1}{\gamma+1}\alpha)}{\sqrt{1+\mu}}$$

---

[1] i.e. the solution of the Riemann problem consisting of either rarefaction waves or contact discontinuities or entropy satisfying shocks.

178

and $\mathbf{V}^{r_1}(\xi, \mathbf{V}^0)$ and $\mathbf{V}^{r_3}(\xi, \mathbf{V}^0)$ are

(16)
$$a^{r_1}(\xi, \mathbf{V}^0) = a^0 - \frac{\gamma - 1}{\gamma + 1}\xi \qquad a^{r_3}(\xi, \mathbf{V}^0) = a^0 + \frac{\gamma - 1}{\gamma + 1}\xi$$
$$u^{r_1}(\xi, \mathbf{V}^0) = u^0 + \frac{2}{\gamma + 1}\xi \qquad u^{r_3}(\xi, \mathbf{V}^0) = u^0 + \frac{2}{\gamma + 1}\xi$$
$$v^{r_1}(\xi, \mathbf{V}^0) = v^0 \qquad\qquad v^{r_3}(\xi, \mathbf{V}^0) = v^0$$
$$s^{r_1}(\xi, \mathbf{V}^0) = s^0 \qquad\qquad s^{r_3}(\xi, \mathbf{V}^0) = s^0.$$

Notice that $\mathbf{V}^{r_1}(0, \mathbf{V}^0) = \mathbf{V}^0$ and $\mathbf{V}^{r_3}(0, \mathbf{V}^0) = \mathbf{V}^0$ and that the parameter ξ is related to the slope $\lambda_i = (x - x_i)/(t - t^n)$, i.e., for a given $t > t^n$, to the x coordinate, through a one-to-one relationship. For the 1 wave one has

(17)
$$\xi = \lambda_i - \lambda_i^{1a} = (u^{r_1}(\xi, \mathbf{V}_i^a) - a^{r_1}(\xi, \mathbf{V}_i^a)) - (u_i^a - a_i^a).$$

Thus $\mathbf{V}^{r_1}(\xi, \mathbf{V}^a)$ is a curve in the phase space as well as a function of x: as ξ varies between zero and α, λ_i varies between $u_i^a - a_i^a$ and $u_i^c - a_i^c$.

Consider the case $\alpha < 0$. In this case $\mathbf{V}_i^c$ lies, in the (x, t) space, to the *left* of $\mathbf{V}_i^a$ (figure 2, left).

In this case if one tries to prolongate, at some fixed time $t = t^n + k$, $k > 0$ $\mathbf{V}^{r_1}(\xi, \mathbf{V}^a)$ with constant states $\mathbf{V}_i^a$ and $\mathbf{V}_i^c$ to the *left* and to the *right* of $x = x_i + \lambda_i^{1a}k$ and $x = x_i + \lambda_i^{1c}k$, respectively, result in a multi-valued "function". This "function" is called a 1 *compression wave* and is sketched in the middle of figure 2.

Clearly a unique solution of the Riemann problem can be recovered by replacing the 1 compression wave with an entropy satisfying shock (figure 2, right) i.e. the function $\mathbf{V}^{r_1}(\xi, \mathbf{V}^a)$ with the Rankine-Hugoniot relationships.
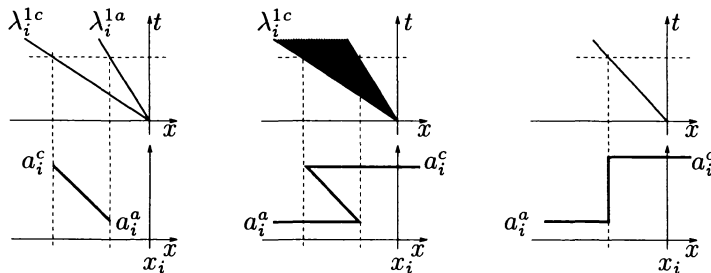

Fig. 2. Function $\mathbf{V}^{r_1}(\xi, \mathbf{V}^a)$ between $\mathbf{V}^a$ and $\mathbf{V}^c$ for $\alpha < 0$ (left); prolongation of $\mathbf{V}^{r_1}(\xi, \mathbf{V}^a)$ by means of a multi-valued wave (middle) and replacement of $\mathbf{V}^{r_1}(\xi, \mathbf{V}^a)$ with an entropy satisfying shock (right).

Similar considerations hold for the case $\beta > 0$ and thus the solution $\mathbf{U}_i(x, t)$ can be computed.

179

Consider, instead, the solution $\widetilde{\mathbf{U}}_i(x,t)$ obtained with (9) i.e. using rarefaction waves without regard to the sign of α and β. Clearly one has $\widetilde{\mathbf{U}}_i(x,t) = \mathbf{U}_i(x,t)$ for $\alpha \geqslant 0$ and $\beta \leqslant 0$. Otherwise $\widetilde{\mathbf{U}}_i(x,t)$ is multi-valued as seen above.

Consider, in particular, the case $\alpha < 0$ and $\beta \leqslant 0$ so that $\widetilde{\mathbf{U}}_i(x,t^n + k)$ is multi-valued for $x - x_i \in [\lambda_i^{1c}k, \lambda_i^{1a}k]$. Let us re-define $\widetilde{\mathbf{U}}_i(x,t^n + k)$ on this subset as follows

(18) $$\widetilde{\mathbf{U}}_i(x,t^n + k) = \mathbf{U}_i^a + \mathbf{U}_i^c - \mathbf{U}(\mathbf{V}^{r_1}(\xi, \mathbf{V}^a))$$

for $x - x_i \in [\lambda_i^{1c}k, \lambda_i^{1a}k]$ $\Leftrightarrow$ $\xi \in [0, -\alpha]$. With this rule and using the fact that $\widetilde{\mathbf{U}}_i(x,t)$ consist of piecewise exact solution of Riemann problems with initial data $(\mathbf{U}_i^c, \mathbf{U}_i^a)$, $(\mathbf{U}_i^c, \mathbf{U}_i^d)$ and $(\mathbf{U}_i^d, \mathbf{U}_i^b)$ one can show (see [3]) that

(19) $$\int_{x_i - h/2}^{x_i + h/2} \widetilde{\mathbf{U}}_i(x,t^n + k)\,\mathrm{d}x = \int_{x_i - h/2}^{x_i + h/2} \mathbf{U}_i(x,t^n + k)\,\mathrm{d}x.$$

This is not surprising because, with (18), the integration path across the compression wave has been chosen in order to enforce conservation (figure 3).
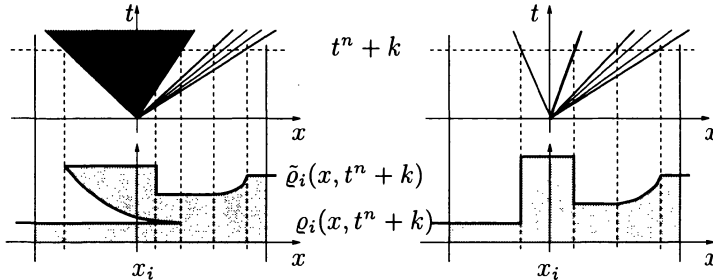

Fig. 3. Multi-valued, *approximate* (left) and *exact* (right) solution of the Riemann problem.

Clearly $\widetilde{\mathbf{U}}_i(x,t^n + k)$ can be re-defined, on the subsets of $[x_i - h/2, x_i + h/2]$ where it is multi-valued, in such a way that (19) holds for the cases $\alpha < 0$, $\beta > 0$ and $\alpha \geqslant 0$, $\beta > 0$ as well.

An approximate Godunov's method can then be derived by simply replacing $\mathbf{U}_i(x,t^n + k)$ with $\widetilde{\mathbf{U}}_i(x,t^n + k)$ on the right hand side of (12) and (13)

(20) $$\mathbf{F}_{i,j} = \widetilde{\mathbf{F}}(\mathbf{U}_{i-1,j}^n, \mathbf{U}_{i,j}^n) = \mathbf{F}(\mathbf{U}_{i-1,j}^n) + \frac{h}{2k}\mathbf{U}_{i-1,j}^n - \frac{1}{k}\int_{x_i - h/2}^{x_i} \widetilde{\mathbf{U}}_i(x,t^n + k)\,\mathrm{d}x$$

or

(21) $$\mathbf{F}_{i,j} = \widetilde{\mathbf{F}}(\mathbf{U}_{i-1,j}^n, \mathbf{U}_{i,j}^n) = \mathbf{F}(\mathbf{U}_{i,j}^n) - \frac{h}{2k}\mathbf{U}_{i,j}^n + \frac{1}{k}\int_{x_i}^{x_i + h/2} \widetilde{\mathbf{U}}_i(x,t^n + k)\,\mathrm{d}x$$

$\widetilde{\mathbf{F}}$ is the *numerical flux function*. Clearly $\widetilde{\mathbf{F}}$ is consistent with $\mathbf{F}$. Notice that the time step k must satisfy a CFL rule as in the original method. Notice that $\mathbf{F}_{i,j}$ cannot, in general, be interpreted as the value of $\mathbf{F}(\widetilde{\mathbf{U}}_i(x,t))$ at $x = x_i$ as the computation of the integrals on the right hand side of (20), (21) shows. This computation depends on the wave configuration issuing from the Riemann problem and give the numerical fluxes of the Flux Difference Splitting method of Pandolfi. For instance one has, for the wave configuration sketched on the left of figure 3

$$(22) \qquad \mathbf{F}_{i,j} = \mathbf{F}(\mathbf{U}_{i-1,j}^n) + \mathbf{F}(\mathbf{U}_i^c) - \mathbf{F}(\mathbf{U}(\mathbf{V}^{r_1}(\xi^*, \mathbf{V}^a)))$$

with $\xi^* = -(u_i^a - a_i^a)$. This is one of the few cases where a *sonic state*, $\mathbf{U}(\mathbf{V}^{r_1}(\xi^*, \mathbf{V}^a))$, must be computed. Notice, however, that the cost of this computation is negligible.

The advantage of the interpretation (20), (21) of Pandolfi's flux function is that the cell averages obtained in each single step of the split method (6) can be interpreted as averages of a function. Consider the x-step. Using (20) and (21), (7) can be written as

$$(23) \qquad I_x(k): \quad \mathbf{U}_{i,j}^n \rightarrow \frac{1}{h} \int_{x_i}^{x_i + h/2} \widetilde{\mathbf{U}}_i(x, t^n + k)\,\mathrm{d}x + \frac{1}{h} \int_{x_i + h/2}^{x_{i+1}} \widetilde{\mathbf{U}}_{i+1}(x, t^n + k)\,\mathrm{d}x.$$

Therefore a discrete entropy inequality

$$(24) \qquad S\left(\mathbf{U}_{i,j}^n - \frac{k}{h}\left[\mathbf{F}_{i+1,j} - \mathbf{F}_{i,j}\right]\right) \geqslant S(\mathbf{U}_{i,j}^n) - \frac{k}{h}\left[H_{i+1,j} - H_{i,j}\right]$$

with $H_{i,j} = \widetilde{H}(\mathbf{U}_{i-1,j}^n, \mathbf{U}_{i,j}^n)$ and $\widetilde{H}$ consistent with $S(\mathbf{U})u(\mathbf{U})$ can be derived for the x-step of the split method (6) if the following inequalities are satisfied

$$(25) \qquad S\left(\frac{1}{b-a}\int_a^b \mathbf{U}(x,t)\,\mathrm{d}x\right) \geqslant \frac{1}{b-a}\int_a^b S(\mathbf{U}(x,t))\,\mathrm{d}x,$$

$$(26) \quad \frac{1}{h}\int_{x_i-h/2}^{x_i+h/2} S(\widetilde{\mathbf{U}}_i(x,t^n+k))\,\mathrm{d}x \geqslant \frac{1}{2}(S_{i-1,j}^n + S_{i,j}^n) - \frac{k}{h}\left[S_{i,j}^n u_{i,j}^n - S_{i-1,j}^n u_{i-1,j}^n\right].$$

In this case the discrete entropy inequality (24) (together with its counterpart for the y-step) can be used to show that for the split method (6) the property (iii) holds.

The point is whether (25) and (26) hold or not. The first inequality, (25), holds because $S(\mathbf{U})$ is a concave function.

Consider inequality (26) and let $\widetilde{\mathbf{U}}_i(x, t^n + k)$ be multi-valued for $x \in [x_i + \lambda_i^{1c}k, x_i + \lambda_i^{1a}k] \subset [x_i - h/2, x_i + h/2]$ as in the case sketched on the left side of figure 3.

In this interval $\widetilde{\mathbf{U}}_i(x, t^n + k)$ must be taken as in (18). One can show that, in this case, (26) holds if

(27) $$s\left(\mathbf{U}_i^a + \mathbf{U}_i^c - \mathbf{U}(\mathbf{V}^{r_1}(\xi, \mathbf{V}_i^a))\right) \geqslant s\left(\mathbf{U}_i^a\right) = s\left(\mathbf{U}_i^c\right)$$

for $\xi \in [\alpha, 0]$. Clearly one has $\mathbf{V}^{r_1}(\alpha, \mathbf{V}^a) = \mathbf{V}_i^c$ and $\mathbf{V}^{r_1}(0, \mathbf{V}^a) = \mathbf{V}_i^a$. Therefore (27) can be written as

(28) $$s\left(\mathbf{U}(\mathbf{V}_i^a) + \mathbf{U}(\mathbf{V}^{r_1}(\alpha, \mathbf{V}_i^a)) - \mathbf{U}(\mathbf{V}^{r_1}(\xi, \mathbf{V}_i^a))\right) - s\left(\mathbf{U}_i^a\right) \geqslant 0 \quad \xi \in [\alpha, 0].$$

The function on the left side of (28) depends on $\mathbf{V}_i^a$ only through the speed of sound a_i^a. Let this function be $\Delta s(a, \alpha, \xi)$. In figure 4 $\Delta s(a, \alpha, \xi)$ has been plotted for $\alpha = -1$ and $a = 1, 1/3, 1/6$ and $1/12$ and $\xi \in [\alpha, 0]$.
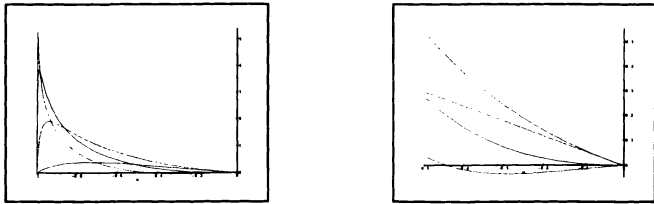

Fig. 4. $\Delta s(a, \alpha, \xi)$: $\alpha = -1$, $a = 1, 1/3, 1/6, 1/12$ and ξ between α and 0 (left) and between -0.5 and 0 (right).

One can clearly see that Δs is always positive except for the case $a = 1/12$. If one computes the first derivative of Δs with respect to ξ at $\xi = 0$, one has

(29) $$\frac{\partial}{\partial \xi} \Delta s(a, \alpha, \xi) \leqslant 0 \iff -6a \leqslant \alpha \leqslant 0$$

for $\gamma = 1.4$. Notice that a compression wave with $\alpha = -6a$ is quite strong. Such a wave accelerates a flow at rest up to Mach numeber 2.5!

The above consideration explain why the numerical method (6) with fluxes given by (20), (21) works well in practice. Notice also that the condition (28) is not necessary for the inequality (26) to hold.

2.2. High resolution method. The main drawback of the method described so far is that it is only first order accurate. A high resolution method based on the numerical flux function (20), (21) can be derived by means of the following two steps:

a) Replace the dimensional splitting (6) with a Strang splitting [18].

182

b) Add to the numerical flux function (20), (21) a limited correction term to obtain, on smooth solutions, a second order numerical flux function.

Consider step b). For the linear case, $\mathbf{F}(\mathbf{U}) = \mathbf{A}\mathbf{U}$, the second order numerical flux function of Lax-Wendroff

$$(30) \quad \widetilde{\mathbf{F}}^{LW}(\mathbf{U}^n_{i-1,j}, \mathbf{U}^n_{i,j}) = \frac{1}{2}\mathbf{A}\left(\mathbf{U}^n_{i-1,j} + \mathbf{U}^n_{i,j}\right) - \frac{k}{2h}\mathbf{A}^2\left(\mathbf{U}^n_{i,j} - \mathbf{U}^n_{i-1,j}\right)$$

can be written as the sum of Godunov's flux function, $\widetilde{\mathbf{F}}^G$, and of a (second order) correction term (see [10]):

$$(31) \quad \widetilde{\mathbf{F}}^{LW}(\mathbf{U}^n_{i-1,j}, \mathbf{U}^n_{i,j}) = \widetilde{\mathbf{F}}^G(\mathbf{U}^n_{i-1,j}, \mathbf{U}^n_{i,j}) + \frac{1}{2}\sum_{w=1}^{nw}|\lambda^w|\,(h - k|\lambda^w|)\,\frac{\mathbf{r}^w\alpha_i^w}{h}.$$

In (31) nw is the number of discontinuities issuing from the solution of the Riemann problem with initial data $\mathbf{U}^n_{i-1,j}$ and $\mathbf{U}^n_{i,j}$. λ^w is the characteristic speed of the w discontinuity and $[\,\mathbf{U}\,]_i^w = \mathbf{r}^w\alpha_i^w$ is the portion of the jump $\mathbf{U}^n_{i,j} - \mathbf{U}^n_{i-1,j}$ occurring over the w discontinuity (λ^w, $w = 1, \ldots, nw$ are the eigenvalues of $\mathbf{A}$ and $\mathbf{r}^w$, $w = 1, \ldots, nw$ is a complete set of eigenvectors of $\mathbf{A}$):

$$(32) \quad \begin{aligned} \mathbf{U}^n_{i,j} - \mathbf{U}^n_{i-1,j} &= \sum_{w=1}^{nw}\mathbf{r}^w\alpha_i^w = \sum_{w=1}^{nw}[\,\mathbf{U}\,]_i^w, \\ \mathbf{F}(\mathbf{U}^n_{i,j}) - \mathbf{F}(\mathbf{U}^n_{i-1,j}) &= \sum_{w=1}^{nw}\lambda^w\mathbf{r}^w\alpha_i^w = \sum_{w=1}^{nw}\lambda^w\,[\,\mathbf{U}\,]_i^w. \end{aligned}$$

Consider the numerical flux given by (20), (21). The numerical flux function $\widetilde{\mathbf{F}}(\mathbf{U}^n_{i-1,j}, \mathbf{U}^n_{i,j})$ can always be written

$$(33) \quad \widetilde{\mathbf{F}}(\mathbf{U}^n_{i-1,j}, \mathbf{U}^n_{i,j}) = \mathbf{F}(\mathbf{U}^n_{i-1,j}) + \sum_{\lambda_i^w < 0}[\,\mathbf{F}\,]_i^w = \mathbf{F}(\mathbf{U}^n_{i,j}) - \sum_{\lambda_i^w > 0}[\,\mathbf{F}\,]_i^w.$$

as in the original Flux Difference Splitting formulation. In (33) $[\,\mathbf{F}\,]_i^w$ is the jump of $\mathbf{F}$ across the wave w issuing from the solution (14) of the one-dimensional Riemann problem at $x = x_i$. λ_i^w is just a number used to associate a sign to each wave. The number of waves, nw, may be greater than the number of components of $\mathbf{U}$ because of the fact that sonic points may be embedded in acoustic waves. In such a case the wave is split into two subwaves having λ_i^w of opposite sign (figure 5). Consider
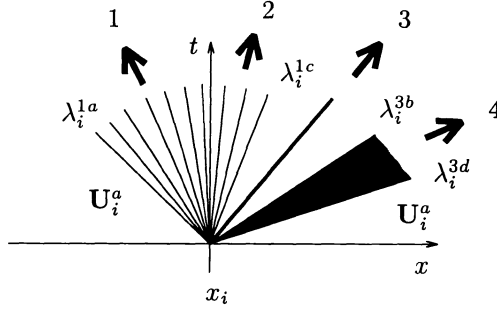
183

Fig. 5. Solution of a one-dimensional Riemann problem with a sonic point embedded in a rarefaction wave.

the jump $[\mathbf{F}]_i^w$. This can always be written as the product of a diagonal matrix $\mathbf{\Lambda}_i^w$ times the jump of $\mathbf{U}$ across the wave w

$$(34) \qquad\qquad [\mathbf{F}]_i^w = \mathbf{\Lambda}_i^w [\mathbf{U}]_i^w.$$

Thus one can think to extend (31) to the non linear case by replacing the Godunov's flux $\mathbf{A}^+ \widetilde{\mathbf{U}}_{i-1,j}^n + \mathbf{A}^- \widetilde{\mathbf{U}}_{i,j}^n$ with the numerical flux function $\widetilde{\mathbf{F}}(\mathbf{U}_{i-1,j}^n, \mathbf{U}_{i,j}^n)$ and λ^w, $\mathbf{r}^w \alpha_i^w$ with $\mathbf{\Lambda}_i^w$ and $[\mathbf{U}]_i^w$ respectively. Let this numerical flux function be $\widetilde{\mathbf{F}}^{hr}$. One has

$$(35) \qquad \widetilde{\mathbf{F}}^{hr}(\mathbf{U}_{i-1,j}^n, \mathbf{U}_{i,j}^n) = \widetilde{\mathbf{F}}(\mathbf{U}_{i-1,j}^n, \mathbf{U}_{i,j}^n) + \frac{1}{2} \sum_{w=1}^{nw} |\mathbf{\Lambda}_i^w| \, (h\mathbf{I} - k|\mathbf{\Lambda}_i^w|) \, \frac{[\mathbf{U}]_i^w}{h}.$$

The correction term on the right hand side of (35) can then be limited by applying some standard slope limiter method to the *slope* $[\mathbf{U}]_i^w/h$ (see [17]).

2.3. Boundary conditions. In the numerical computation of flows of practical relevance the problem of the treatment of the boundaries cannot be avoided.

For *natural* boundaries, such as walls, the numerical fluxes can be easily computed. Consider the last interface in the x direction: $x = x_{ni}$, $y \in [y_j, y_j + h]$. The numerical flux $\mathbf{F}_{ni,j}$ is formally given by (35)

$$(36) \qquad\qquad \mathbf{F}_{ni,j} = \widetilde{\mathbf{F}}^{hr}(\mathbf{U}_{ni-i,j}^n, \mathbf{U}_{ni,j}^n).$$

Notice, however, that $\mathbf{U}_{ni,j}^n$ represents a state outside the computational domain $\mathscr{D}$. It is easy to see that $\mathbf{U}_{ni,j}^n$ can be computed, on the basis of $\mathbf{U}_{ni-i,j}^n$, in such a way that the boundary condition

$$(37) \qquad \mathbf{u}(\mathbf{U}_i(x_i, t)) \cdot (1,0) = 0 \quad \text{for} \quad t \in [t^n, t^n + k] \quad \Rightarrow \quad u_{ni}^c = u_{ni}^d = 0$$

184

is satisfied. Therefore the Riemann problem at $x = x_{ni}$ can be solved and the numerical flux computed as for an internal interface.

For *computational* boundaries such as inflow or outflow sections (duct flows) and outer boundaries (external flows) the problem of the enforcement of a proper boundary condition is more complex. This problem has been discussed in [3]. See also [14].

3. VALIDATION

The problem of verifying the correctness of a numerical method and of its implementation is not a trivial one. This is essentially because of two reasons.

The first reason is that there are only very few cases (see 3.1) for which an exact solution of the Euler equations is available.

The second reason is that it is not possible to know, a-priori, whether the comparison between numerical results and experimental data (such as those obtainable through wind tunnel measurements, for instance) makes sense or not. This is because of the fact that the viscosity (physical as well as numerical) affects the behaviour of the flow both quantitatively and qualitatively.

The qualitative influence of viscosity is related to the stability properties of a given *basic* flow. In [3] it was shown that a wide class of two- and three-dimensional inviscid steady flows are unstable. Would this be the case if viscosity were accounted for? The point is that there are many instability mechanisms and it is not always clear whether viscosity has, for a given basic flow, a stabilizing or a destabilizing effect. It is well known (see [7]) that, even if in many cases the viscosity tends to damp instabilities, nevertheless there are flows where an instability arises because of the transport of momentum in the direction normal to the velocity vector.

Therefore, for cases where no exact solution of the Euler equations is known, the comparison of numerical results with experimental data should not be regarded, in general, as an alternative way to validate a numerical method.

A true alternative to the comparison with the exact solution consists in checking the consistency between the numerical results and the governing equations themselves. For instance total enthalpy gradients must be identically zero in steady homenergic flows. For such flows a discrete form of the total enthalpy gradient could be used as an indicator of the errors introduced by the discretization. In a similar way entropy can be used to monitor the quality of a numerical solution of steady homentropic smooth flows ([2]).

Another way to validate a numerical method is to compare the results with those obtained with other numerical techniques and with the same discretization and the same initial and boundary conditions. In practice one compares the results obtained

185

with the method to be validated with some "reference solution" or with a collection of other numerical results. For the test cases discussed in sections 4 and 5, for instance, well established reference solutions have existed since about ten years and have been widely used to test many new numerical methods.

The approaches outlined above, *comparison with an exact solution*, *comparison with other numerical computations* and *check of consistency with the governing equations*, are, together with the standard practice of comparing numerical results obtained with different space and time discretizations, the essentials of the validation methodology used here.

3.1. One-dimensional and quasi one-dimensional cases. The major goal of these computations is to test the numerical method described in section 2 with respect to the following issues:

- capability of the method to capture shocks and contact discontinuities with a good resolution.
- accuracy of the method
- correctness of the boundary conditions and capability of the method to describe the behaviour of the flow at large times

In the following, numerical results for the pure one-dimensional case will be presented and discussed. For a critical comparison between the results obtained with the method (and with other numerical techniques) and the exact solution see, for the quasi one-dimensional case (nozzle flows), [4]. Consider figure 6 below.
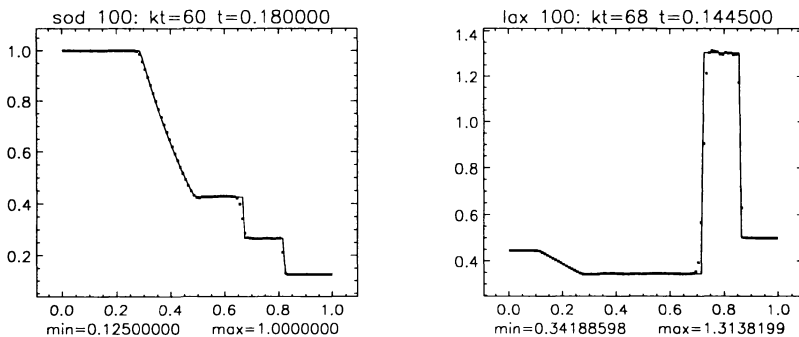

Fig. 6. Shock tube: **density** distribution for Sod's (left) and Lax's (right) problems; 100 cells; high resolution method with the "superbee" limiting function of Roe.

On the left side the numerical solution (dots) obtained with the high resolution method for the Riemann problem with initial condition given in table 1 have been drawn together with the exact solution (continuous line). The time is $t = 0.18$. The

186

interval $[0, 1]$ has been discretized into 100 regular cells. The time step was .003. Notice that both the shock (the discontinuity at $x \approx 0.8$ in figure 6 left) and the contact discontinuity are captured without (or with very weak) spurious oscillations. The shock is smeared over two computational cells. For the description of the contact discontinuity four cells are needed.

On the right side of figure 6 the results obtained for the Riemann problem defined in table 2 and using the same space discretization of 100 cells are shown. The time is now 0.1445 and the time step 0.0017. For this test case three lls are needed to describe the rightward moving shock (at $x \approx 0.85$) and five for the contact discontinuity.

Sod's problem
$(\varrho, u, p)(x, 0) = \begin{cases} (1, 0, 1) & \text{if } x < 0.5, \\ (0.125, 0, 0.1) & \text{if } x > 0.5. \end{cases}$

Table 1. Sod's problem: initial data

Lax's problem
$(\varrho, u, p)(x, 0) = \begin{cases} (0.445, 0.698, 3.528) & \text{if } x < 0.5, \\ (0.5, 0, 0.571) & \text{if } x > 0.5. \end{cases}$

Table 2. Lax's problem: initial data

The numerical results shown in figure 6 are comparable with the results obtained by Chang and Liou in [5]. In their work Chang and Liou compared the ENO (Essentially Non Oscillatory) scheme of Harten, Engquist, Osher and Chakravarthy and the TVD (Total Variation Diminishing) scheme of Liou. In the computations shown in figure 6, as well as in those of Chang and Liou, the "superbee" limiting function of Roe ([16]) has been used.

It is worth to stress the fact that the choice of the limiting function has a tremendous effect on the quality of the description of the contact discontinuity. This can be seen from the comparison between figure 6 and figure 7 where the same computations have been made using the limiting function of van Leer. In the last computation six and eight computational cells are needed for the description of the contact discontinuity in Sod's and Lax's problems, respectively.

Notice, however, that the small oscillations characterizing the numerical solution of figure 6 now completely disappeared in figure 7.

Before going to the next test case let us turn the attention to the second point mentioned at the beginning of this section: the accuracy of the scheme. Consider again Sod's problem. The one-norm of the density error in the rarefaction wave (h
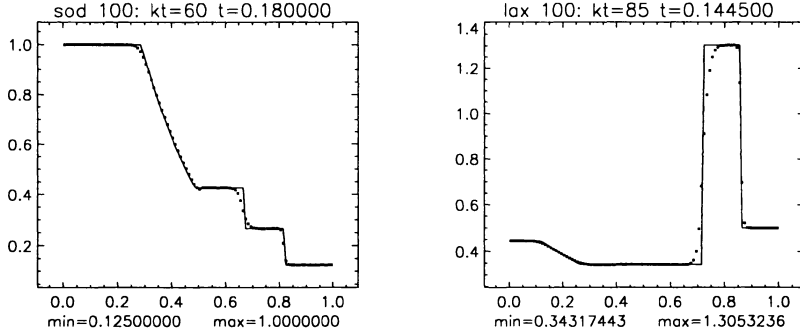
Fig. 7. Shock tube: **density** distribution for Sod's (left) and Lax's (right) problems; 100 cells; high resolution method with limiting function of van Leer.

is as usual the length of the computational cells)

$$E_\varrho^h = h \sum_{\substack{x_i > 0.3 \\ x_i < 0.47}} |\varrho_i^h - \varrho_i^0| \quad x_i = (i - 0.5)h, \quad i = 1, \ldots, \frac{1}{h}$$

has been computed for $h = .01$, $h = .005$ and $h = .0025$ for the high resolution as well as for the approximate Godunov's method. These errors, multiplied by 1000, are reported in table 3, left.

These results give a convergence rate of about one for the high resolution method and of about 0.65 for the approximate Godunov's method. Notice, however, that for the smooth flow of initial data

$$\varrho = 1, \ p = 1, \ u(x,0) = \begin{cases} -0.5 & \text{if } x \leqslant 0.4, \\ 0.5 \sin\left((x - 0.5)\pi/0.2\right) & \text{if } 0.4 < x < 0.6, \\ 0.5 & \text{if } x \geqslant 0.6. \end{cases}$$

the same methods give convergence rates of about 1.8 and one, respectively (table 3, right). For this last case the error has been measured with respect to a computation with $h = .0003125$ (3200 cells).

h	hrm	Gv's
.01	.6429	4.6911
.005	.3129	3.0638
.0025	.1530	1.9208

h	hrm	Gv's
.01	.2885	2.7696
.005	.08562	1.4218
.0025	.02566	0.7229

Table 3. Sod's problem (left) and smooth flow (right): density error (one norm) for the high resolution method with the "superbee" limiting function (hrm) and the approximate Godunov's method (Gv's)

The error analysis shows the following

- The accuracy of the high resolution method does not exceed one on the smooth part of the flow if the initial conditions are not smooth. The method behaves as expected (i.e. with convergence rate of about two) for smooth initial data (and as long as the solution remains smooth, of course).

- With meshes of practical interest (for one-dimensional shock tubes typically consisting of about 100 cells) the error of the numerical solution obtained with the high resolution method is about one order of magnitude less than the one affecting the approximate Godunov's computation.

The above consideration close the discussion about the first two issues, shock capturing capability and accuracy, discussed in this section.

In the numerical results presented above the boundary conditions did not play any role because the interest was focused on the behaviour of the flow shortly after the beginning of the integration. In order to check the boundary conditions at inflow and outflow boundaries and the capability of the numerical method to correctly describe the behaviour of the flow at large times, the following test problem has been conceived.

Imagine a shock tube set-up. Let the tube be filled with gas at rest ($u = 0$). Let the pressure and the density of the gas be constant and equal to one. Let the right-end of the tube be closed by a wall. The left-end is separated from the environment by means of a diaphragm (figure 8 top left). The environment is a huge reservoir at pressure 0.9 and density equal to one. The speed of the flow in the reservoir is zero (except for the immediate neighborhood of the section where the reservoir is connected with the left-end of the tube).
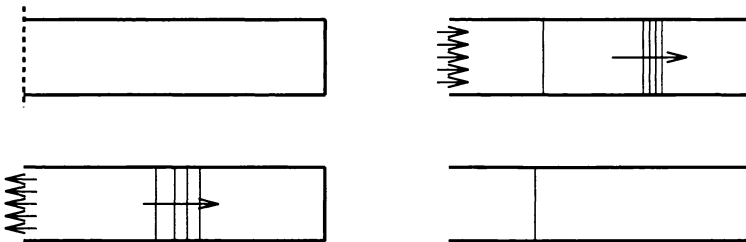

Fig. 8. Discharge of a one-dimensional tube into a reservoir; rarefaction wave (r.w.), compression wave (c.w.), contact discontinuity (c.d.).

At $t = 0$ the diaphragm is broken. A rightward running rarefaction wave is generated at the left-end of the tube. This is a 3 rarefaction wave and, since the speed of the flow in the tube is zero (because of the initial condition), the velocity

of the gas behind the rarefaction wave must be negative, i.e. from right to left. The gas flows out of the tube (figure 8 bottom left).

The rightward running rarefaction wave hits the wall at the right-end of the tube and is reflected. The reflected wave is still a leftward running rarefaction wave. As this rarefaction wave reaches the open boundary at the left-end of the tube (which is meanwhile an *outlet* boundary), it is reflected as a compression wave. A 3 compression wave propagating into a gas at rest induces, behind itself, a positive velocity. The left-end of the tube must be now an *inlet* boundary and a contact discontinuity travels into the tube (figure 8 top right).

The process continues until the pressure in the tube has reached a uniform value of 0.9 and the speed of the flow is uniformly zero. This happens asymptotically for $t \to \infty$. At this stage a portion of the gas initially contained in the tube has flown out of it and some gas of the environment flew into the tube. These two gases are separated by a steady contact discontinuity (figure 8 bottom right).

The numerical results relative to this computation have been drawn in an (x, t) diagram in figure 9. The very beginning of the transient is shown on the top and the almost steady state reached after 400 time units on the bottom of the picture. The left side represents the results obtained with the approximate Godunov's method. The results obtained with the high resolution method are shown on the right.

Notice the correctness of the treatment of the left-end boundary and, in the computation with the high resolution method, the sharpness of the contact discontinuity issuing from that boundary at $t \approx 1.7$.

The difference in the description of this contact discontinuity is indeed the most striking difference between the two computations. The major weakness of the approximate Godunov's method is not the fact that it smears the contact discontinuity over many computational cells in comparison with the high resolution method. The problem with the lower order method is that it even fails to propagate such a poor description in time (notice the divergence of the contour lines of the contact discontinuity in figure 9 top left).

The consequences of such a weakness can be clearly seen in the large time behaviour of the flow. The approximate Godunov's method provides, at $t = 400$, a density distribution smoothly varying over the whole length of the tube. With the high resolution method, on the contrary, the contact discontinuity separating the gas coming from the environment from the gas initially filling the tube is correctly captured at $t = 400$ and even at larger times.
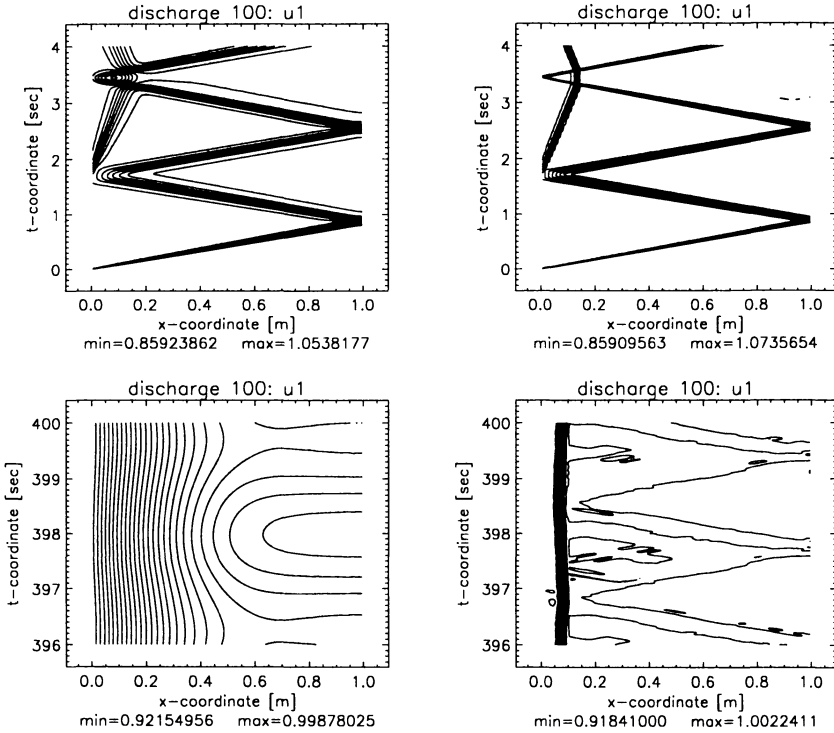
Fig. 9. Discharge of a one-dimensional tube into a reservoir: (x, t) diagrams of **density** at the very beginning of the transient (top) and after 400 time units (bottom); approximate Godunov's method (left) and high resolution method (right).

4. MACH 3 TUNNEL WITH A STEP

The goal of these computations is to validate the numerical method in the two-dimensional case. The attention is focused on the following issues:
- Behaviour of the method on a regular, Cartesian mesh.
- Entropy generation at singular points.
- Instability of steady contact discontinuities.

The test case is the one re-proposed, in 1982, by Woodward and Colella. A wind tunnel with a forward facing step at Mach number equal to 3 (figure 10 left). For a detailed description of the geometry of the tunnel and of the initial and boundary conditions see [19].

In order to compare the numerical results obtained here with those presented in [19], the same special treatment of the expansion corner has been introduced (figure 10 right). At the end of each integration step the values of the density and of the magnitude of the velocity vector of the cells marked with a cross have been
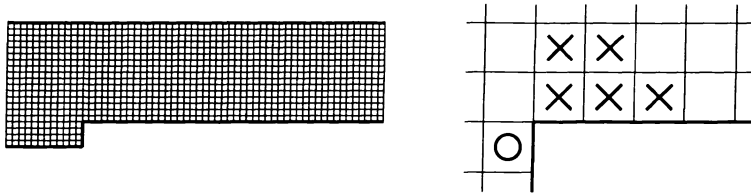
Fig. 10. The Mach 3 tunnel with a step (left) and the special treatment of the expansion corner (right).

reset. The new density has been computed with the pressure (which is not changed) and with the entropy of the cell marked with a circle. The modulus of the velocity vector has been computed with the total enthalpy of the cell marked with a circle, with the pressure and with the already corrected density.

In figure 11 the numerical results obtained with the approximate Godunov's method (left) and with the high resolution method (right) at $t = 4$ are shown for three different meshes.

The results obtained with the high resolution method have been computed with the limiting function of van Leer and are comparable with those reported in [19] for the MUSCL (Monotonic Upwind Scheme for Conservation Laws) of van Leer and for the PPM (Piecewise Parabolic Method) of Woodward and Colella.

approx. Godunov's 40x120 t=4 : u1   high resolution 40x120 t=4 : u1

approx. Godunov's 80x240 t=4 : u1   high resolution 80x240 t=4 : u1

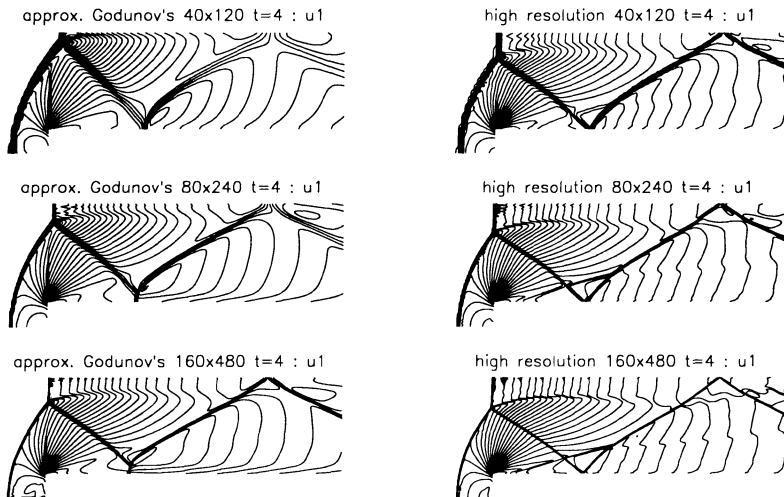approx. Godunov's 160x480 t=4 : u1   high resolution 160x480 t=4 : u1

Fig. 11. Mach 3 wind tunnel with a step: **density** contour lines; approximate Godunov's (left) and high resolution method (right).

The relevant point here is the difference between the results obtained with the approximate Godunov's and with the high resolution method and, in particular, the

difference in the description of the flow about the singular corner and of the wall-shock interaction downstream of the corner. The disturbing fact is that the difference between the two numerical solutions does not seem to vanish as the mesh is refined. On the contrary the irregular reflection in the low order computation strengthens as the cell size diminishes. The same can be said of the oblique shock that can be observed to form just downstream of the expansion corner in the solution obtained with the high resolution method: the two computations seem to converge, as the grid size tends to zero, toward two different numerical solutions.

The explanation for the divergent behaviour of the solutions obtained with the approximate Godunov's and with the high resolution method can be found in the erroneous generation of entropy in the cells just after the expansion corner (except for the cells whose values of entropy and total enthalpy have been reset, of course). This can be clearly seen in figure 12 where the entropy distribution along the first row of cells above the corner has been drawn.

With the approximate Godunov's method (figure 12, left) entropy is generated in the first cells just downstream of the specially treated ones (these can be easily identified in the figure: they are the three cells at $x \approx 0.6$ which carry exactly the same entropy value).

The erroneously generated entropy is advected downstream. The interaction, between such high entropy levels (values greater than 0.8) and the shock wave issuing from the triple point of the main shock on the left of the tunnel, generates the irregular Mach reflection at the bottom wall of the tunnel. Also with the high resolution method entropy is generated downstream of the expansion corner (figure 12, right). In this case, however, the spurious entropy is not simply advected downstream. In the computation with 80×240 cells and, more clearly, in the one with 160×480 cells, one can see a peak in the entropy distribution just after the expansion corner (figure 12 right: middle and bottom). Downstream of such a peak low values of the entropy are recovered. Such low entropy levels allow a regular reflection of the shock impinging on the wall at the bottom of the tunnel.

The peak in the entropy distribution along the wall is consistent with the structure of the solution shown in figure 11: the velocity vector must have a component directed toward the bottom wall. Such a component generates the oblique shock (which forces the flow to comply with the boundary condition) and advects a low entropy flow toward the wall. Figure 13 shows that this interpretation is correct.

Notice that, both with the approximate Godunov's method and with the high resolution method the spurious entropy generation increases with diminishing cell size. Such pathological behaviour can be seen in figure 12 and, for the high resolution method, in the entropy distribution shown in figure 14, computed on a discretization

of 320×960 cells. There one can see that the peak in the entropy distribution has attained a value of about 1.8.

The pathological behaviour described above eventually leads to the breakdown of the high resolution computations: for some critical value of the cell size the peak in the entropy distribution reaches such a value that the density becomes negative and the computation breaks down. The critical cell size depends, in a very sensitive way, on the choice of the limiting function.

From the above considerations it is clear that, as far as the description of the flow about the singular corner is concerned, both the approximate Godunov's method and the high resolution method produce numerical solutions which are not consistent with
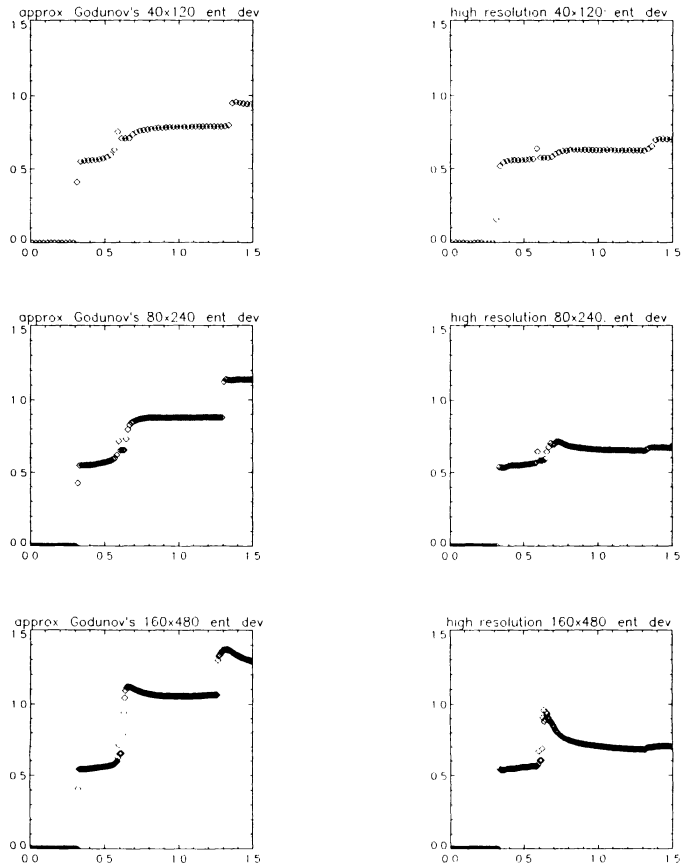

Fig. 12. Mach 3 wind tunnel with a step: **entropy deviation** distribution along the first row of cells above the corner; approximate Godunov's method (left) and high resolution method (right).

194

the governing equations (entropy should not be generated in expansion processes) in the sense that, in both cases, the numerical solutions cannot be expected to converge, for the cell size → 0, to a weak solution of the conservation laws.
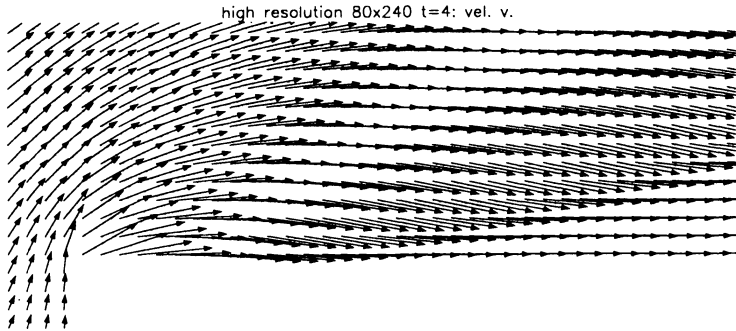
high resolution 80x240 t=4: vel. v.

Fig. 13. Mach 3 wind tunnel with a step: **velocity** field past the expansion corner; high resolution method; 80 × 240 cells.
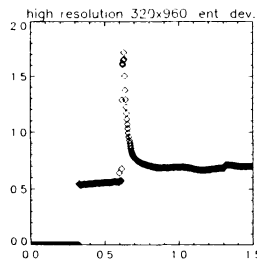
high resolution 320x960 ent. dev.

Fig. 14. Mach 3 wind tunnel with a step: **entropy deviation** distribution along the first row of cells above the corner; high resolution method; 320 × 960 cells.

Before turning the attention to the next validation test, consider figure 15. This shows the contour lines of the density and of the pressure coefficient obtained with the high resolution method on a discretization of 320 × 960 cells. Notice that the contact discontinuity issuing from the triple point assumes, at a certain distance downstream of that point, a wavy shape (figure 15 left). This is a clear symptom of a Kelvin-Helmholtz instability acting on the contact discontinuity.

This contact discontinuity is almost steady and, as one can see from figure 15 right, the pressure varies along the discontinuity. As explained in [3] such kind of discontinuities are locally unstable and decay in a row of vortexes.

This behaviour can be clearly seen in figure 16 where a close-up of the region where the oblique shock hits the upper wall of the tunnel is shown. The variable is
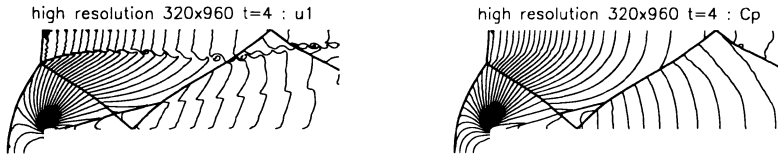
high resolution 320x960 t=4 : u1

high resolution 320x960 t=4 : Cp

Fig. 15. Mach 3 wind tunnel with a step: **density** (left) and **pressure coefficient** (right) contour lines; high resolution method; 320 × 960 cells.

the entropy deviation. The row of vortexes separates the region into two parts. In the upper part the entropy gradients should be identically zero. The entropy spots appearing in this region are a consequence of the grid alignment effect acting on the Mach stem on the left side of the tunnel (not visible in figure 16). Notice the weak interaction between the impinging shock and the row of vortexes.
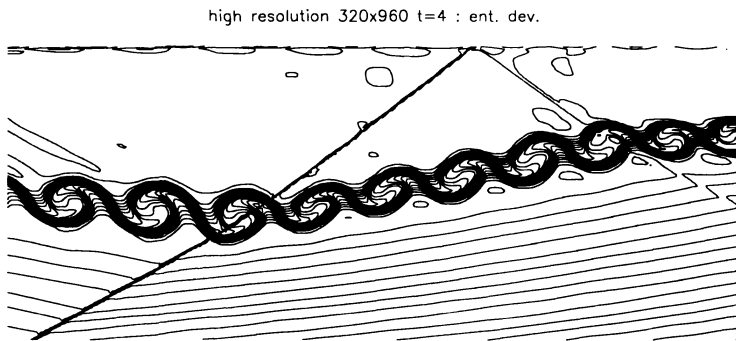

high resolution 320x960 t=4 : ent. dev.

Fig. 16. Mach 3 wind tunnel with a step: **entropy deviation** contour lines; high resolution method; 320 × 960 cells.

5. NACA0012 AT MACH 0.85 AND ONE DEGREE OF INCIDENCE

This problem was proposed to the participants to the GAMM workshop of Rocquencourt[2] with the main goal to investigate the sensitivity of the global coefficients (lift, drag and moment coefficient) with respect to the numerical method and to the space discretization. For a detailed description of the problem see [6]. Here this test case has been used to validate the high resolution method on a curvilinear orthogonal discretization (figure 17).

The grid, obtained from a regular, Cartesian discretization by means of conformal mapping techniques, consists of 32 × 128 computational cells. It is a "C" grid, with

[2] GAMM Workshop on the Numerical Simulation of Compressible Euler Flows, INRIA Rocquencourt, June 10–13, 1986
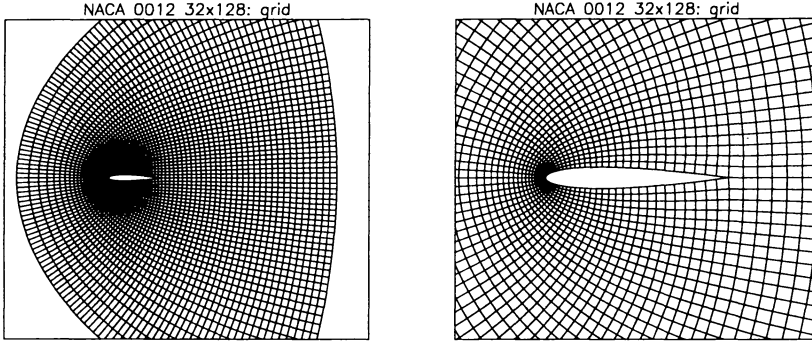
196

Fig. 17. NACA0012: discretization with a "C" grid consisting of 32 × 128 cells.

a cut beginning at the trailing edge of the airfoil. The number of cells lying on the surface of the airfoil is 64; 32 rows of cells are clustered between the airfoil and the far-field and on the two sides of the cut behind it. The initial condition is the undisturbed flow. The numerical results, pressure coefficient and Mach number contour lines, are given on the left side of figure 18. On the right side the corresponding distributions over the first row of cells at the surface of the airfoil are shown.

These results are in good agreement with those presented in [6] by many authors. The value of the lift and drag coefficients, 0.357 and 0.0579 respectively, are in good agreement with the results of Couailler et al. (0.357 and 0.0555), Dadone et al. (0.357 and 0.0596), Hemker et al. (0.356 and 0.0582), Pandolfi et al. (0.359 and 0.0514) and Satofuka et al. (0.357 and 0.0578) discussed in [6].

6. CIRCULAR CYLINDER AT MACH 0.38

The main goal of this section is to quantify the errors due to discretization for the case of a two-dimensional smooth flow and with a curvilinear (polar) orthogonal discretization.

As the NACA0012 problem, the flow about a circular cylinder at $M_\infty = 0.38$ was one of the tests proposed in the GAMM workshop of Rocquencourt. For the cylinder the mesh was given and consisted of 32 cells in the radial direction and of 128 cells in the circumferential direction. The cells are equally spaced circumferentially and clustered radially on the cylinder according to the rule

$$(38) \qquad r_1 = .5 \qquad r_j = .5\left(1 + \sum_{k=0}^{j-2} \alpha^k \frac{2\pi}{nc1}\right) \qquad j = 2, \ldots, nc2 + 1$$

with $nc1 = 128$, $nc2 = 32$ and $\alpha = 1.1648336$. Thus the cells at the surface of the cylinder, r_1, are almost squares and the outer radius, r_{nc2+1}, is equal to 20. Besides
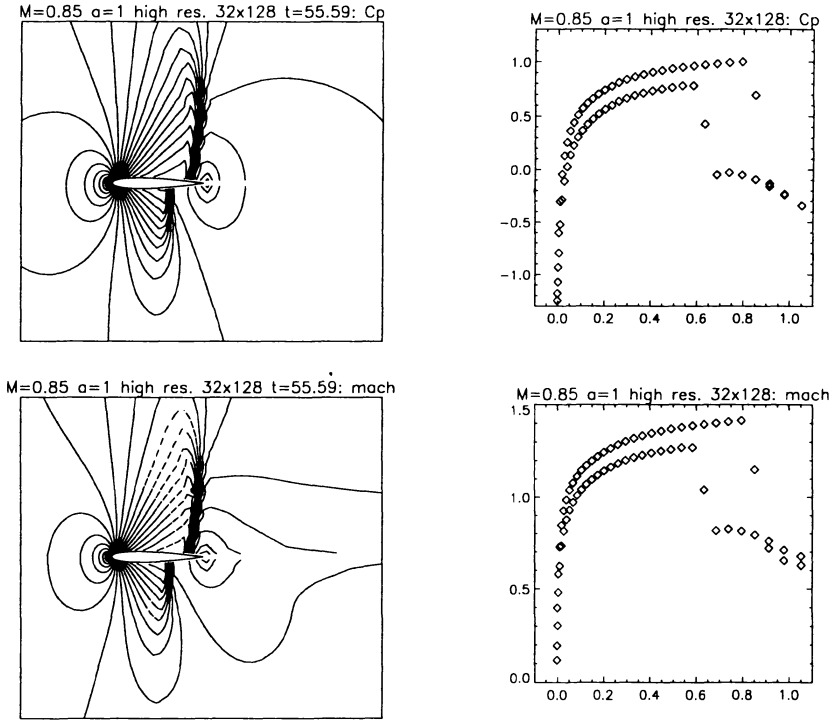
Fig. 18. NACA0012 at $M_\infty = 0.85$ and one degree of incidence: **pressure coefficient** (top) and **Mach number** (bottom) contour lines and values in the first row of cells (airfoil); high resolution method; 32×128 cells.

this standard mesh, say D0, two other grids, consisting of 64×256 (D1) and 128×512 (D2) cells have been used. These are defined as in (38) with $nc1 = 256$, $nc2 = 64$, $\alpha = 1.078449345$ and $nc1 = 256$, $nc2 = 64$, $\alpha = 1.038290107$, respectively.

The initial condition is simply the undisturbed flow at $M_\infty = 0.38$ and pressure and density equal to one. The boundary conditions are those described in section 2.3.

For the cylinder at $M_\infty = 0.38$ the highest value of the local Mach number is below one. Thus a steady, homenergic and homentropic solution can be computed by solving the velocity potential equation (see for instance [1])

$$(39) \qquad (a^2 - \varphi_x^2)\varphi_{xx} - 2\varphi_x\varphi_y\varphi_{xy} + (a^2 - \varphi_y^2)\varphi_{yy} = 0$$

with boundary conditions

$$(40) \qquad \begin{aligned} \nabla\varphi \cdot \mathbf{n} &= 0 \quad \text{for} \quad x^2 + y^2 = 0.25 \\ \varphi &\to u_\infty x \quad \text{for} \quad x^2 + y^2 \to \infty \end{aligned}$$

198

and with $a = a(\varphi_x^2 + \varphi_y^2; h_\infty^o)$. In (39) and (40) φ is the velocity potential and a is the local speed of sound. Because of the above assumptions, a depends only on the local velocity and on the values of the total enthalpy h_∞^o of the undisturbed flow. It is easy to see that, if a unique solution of (39), (40) exists, then this solution is symmetric with respect to the x as well as to the y axis in the sense that[3]

$$\varphi_x(-x,y) = \varphi_x(x,y), \quad \varphi_x(x,-y) = \varphi_x(x,y),$$
(41)
$$\varphi_y(-x,y) = -\varphi_y(x,y), \quad \varphi_y(x,-y) = -\varphi_y(x,y).$$

Consider figure 19. The contour lines of the Mach number for the computations made on the D0 and on the D2 meshes are shown at time $t = 999.5$ and $t = 122.1$ respectively. At such large times the flow has reached a steady state. Notice that both numerical solutions are symmetric with respect to the x axis. However, a significant asymmetry with respect to the y axis can be observed. This is a measure of the error introduced by the discretization. As expected such an error is less noticeable in the computation made with the finer grid (right).
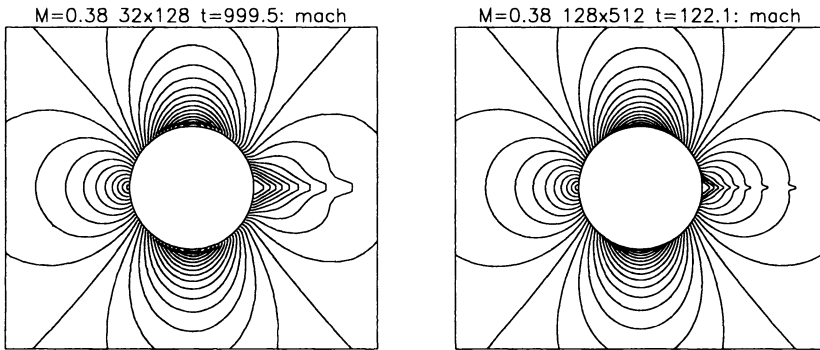

M=0.38 32x128 t=999.5: mach   M=0.38 128x512 t=122.1: mach

Fig. 19. Circular cylinder at $M_\infty = 0.38$: **Mach number** contour lines; 32×128 (left) and 128×512 cells (right).

This is also evident in the diagrams of figure 20 where the entropy (left) and the total enthalpy deviation (right) along the first row of cells surrounding the cylinder are plotted against the x coordinate of the centers of such cells. The three plots in each picture correspond to the computations made with the discretization D0, D1 and D2. All computations have been made with the high resolution method and with the limiting function of van Leer.

---

[3] Let φ be the solution of (39) with boundary conditions (40). Consider the function $\psi(x,y) = -\varphi(-x,y)$. It is easy to see that φ is a solution of (39) and satisfies the boundary conditions (40). Thus $\varphi(x,y) = -\varphi(-x,y)$. Differentiating with respect to x and with respect to y one has (41).

The numerical results presented above are very poor if compared with those that can be obtained, for this test problem, with numerical methods based on other forms of the governing equations. The λ-scheme of Moretti[4], for instance, used by Pandolfi and Larocca in their hybrid "λ-Flux Difference Splitting method", provides, on the 32×128 grid, an almost symmetric solution. The entropy deviation is of course identically zero and the maximum value of the total enthalpy deviation is about 10^{-4}. The drag coefficient (zero in the exact solution) is about .002. In the results presented above the drag coefficient is 0.105 for the same mesh.

In the comparison with other numerical methods based on the conservative form of the governing equations, however, the numerical results obtained with the high resolution method clearly stand out. In [11] Di Mascio shows, for the same problem and with the mesh D0, a maximal value of the entropy deviation of about 0.01. The result was obtained with a finite volume method based on a second order predictor-corrector scheme. Again Di Mascio reports the results obtained with a first order approximate Godunov's method, a maximal value of the entropy deviation of about 0.1, and those obtained with a MUSCL approach, a maximal value of about 0.03. In the above computations (figure 20, left) the maximal value of the entropy deviation is, for the mesh D0, about 0.005. A maximal entropy deviation of about 0.004 was obtained by A. Lerat and J. Sidès with an implicit method (see [6]).
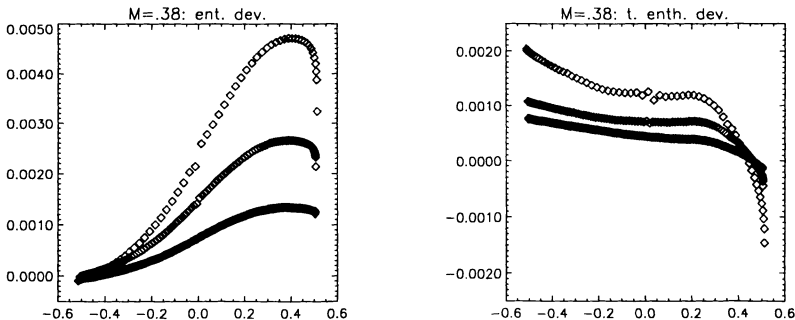

Fig. 20. Circular cylinder at $M_\infty = 0.38$: **entropy deviation** (left) and **total enthalpy deviation** (right); 32×128, 64×256 and 128×512 cells.

---

[4] The λ-scheme of Moretti is based on a characteristic form of the governing equations and on shock fitting techniques for the explicit computation of discontinuities, see [12], [13]

References

[1] *J.D. Anderson*: Modern Compressible Flow. McGraw-Hill Book Company, 1982.

[2] *J.G. Andrews*: Spurious entropy generation as a mesh quality indicator. Report Number 93/12. Oxford University Computing Laboratory, Numerical Analysis Group, 1993.

[3] *N. Botta*: Numerical investigations of two-dimensional Euler flows. PhD thesis. submitted to the Swiss Federal Institute of Technology, 1994.

[4] *N. Botta and J. Sesterhenn*: Deficiencies in the numerical computation of nozzle flow. Research Report No. 92-05. Seminar für Angewandte Mathematik, ETH Zürich, 1992.

[5] *S.-H. Chang and M.-S. Liou*: A numerical study of ENO and TVD schemes for shock capturing. NASA Technical Memorandum 101355. ICOMP-88-18, 1988.

[6] *A. Dervieux, B. Van Leer, J. Periaux and A. Rizzi, editors*: Numerical simulation of compressible Euler flows. Notes on Numerical Fluid Mechanics. volume 26, Proceedings of the GAMM Workshop on Numerical simulation of compressible Euler flows, held at INRIA, Rocquencourt, June 10–13, 1986, Vieweg Verlag, 1989.

[7] *P.G. Drazin and W.H. Reid*: Hydrodynamic Stability. Cambridge University Press, Cambridge, 1981.

[8] *S.K. Godunov*: Finite difference method for numerical computation of discontinuous solutions of the equations of fluid dynamics. Mat. Sbornik *47* (1959). (In Russian.)

[9] *R.J. LeVeque*: Hyperbolic conservation laws and numerical methods. Technical Report No. 90-3. University of Washington, 1990.

[10] *R.J. LeVeque*: Simplified multi-dimensional flux limiter methods. to appear in the Proceedings of the ICFD Conference on Numerical Methods for Fluid Dynamics, Reading, U.K., April, 1992.

[11] *A. DiMascio*: Simulazione di flussi vorticosi mediante il modello di fluido compressible non viscoso. PhD thesis. Universitá "La Sapienza", Roma, Italy, 1992.

[12] *G. Moretti*: The λ-scheme. Comput. Fluids *7* (1979), 191–205.

[13] *G. Moretti*: A technique for integrating two-dimensional Euler equations. Comput. Fluids *15* (1987), no. 1, 59–75.

[14] *G. Moretti and M. Pandolfi*: Critical study of calculations of subsonic flows in ducts. AIAA Journ. *19* (1981), 449–457.

[15] *M. Pandolfi*: A contribution to the numerical prediction of unsteady flows. AIAA Journ. *22* (1984), no. 5, 602.

[16] *P.L. Roe*: Some contributions to the modeling of discontinuous flows. Lecture Notes in Appl. Math. *22* (1985), 163–193.

[17] *C.W. Schulz-Rinne*: The Riemann problem for two-dimensional gas dynamics and new limiters for high-order schemes. PhD thesis. Swiss Federal Institute of Technology, Diss. ETH No. 10297, 1993.

[18] *G. Strang*: On the construction and comparison of difference schemes. SIAM J. Numer. Anal. *5* (1968), 506–517.

[19] *P.R. Woodward and P. Colella*: The numerical simulation of two dimensional fluid flow with strong shocks. J. Comput. Phys. *54* (1984), 115–173.

Authors' address: Nocola Botta, Rolf Jeltsch, Seminar für Angewandte Mathematik, Eidgenössische Technische Hochschule, CH-8092 Zürich, Switzerland.